Ab initio calculation of shocked xenon reflectivity

G. Norman,[1,2] I. Saitov,[1,*] V. Stegailov,[1,2,3] and P. Zhilyaev[1,2]

[1]*Joint Institute for High Temperatures of RAS, Izhorskaya st. 13 Bld. 2, Moscow 125412, Russia*

[2]*Moscow Institute of Physics and Technology (State University), Institutskiy per. 9, Dolgoprudny, Moscow Region 141700, Russia*

[3]*National Research University Higher School of Economics, Myasnitskaya st. 20, Moscow 101000, Russia*

(Received 21 June 2014; published 23 February 2015)

Reflectivity of shocked compressed xenon plasma is calculated within the framework of the density functional theory approach. Dependencies on the frequency of incident radiation and on the plasma density are analyzed. The Fresnel formula for the reflectivity is used. The longitudinal expression in the long-wavelength limit is applied for the calculation of the imaginary part of the dielectric function. The real part of the dielectric function is calculated by means of the Kramers-Kronig transformation. The results are compared with experimental data. The approach for the calculation of plasma frequency is developed.

DOI: 10.1103/PhysRevE.91.023105 PACS number(s): 52.25.−b, 52.25.Mq, 31.15.−p, 71.15.Mb

I. INTRODUCTION

Measurements and theoretical analysis of reflectivity are conventional methods of phase diagram investigations for various substances [1–10], particularly in shock-wave experiments, where the number of the parameters measured is restricted. For instance, the jump of the reflectance in shock compressed liquid deuterium is observed in Ref. [1]. Such an abrupt change of the reflectance from 3.5% to 65% in the pressure range from 0.22 to 0.55 Mbar reveals the onset of the conducting fluid state. The Drude theory [11,12] is used in Ref. [2] for the description of conductivity. By means of this theory, it is shown that the jump of the reflectance is directly related to the increase of the free-charge-carrier density by 7–8 orders of magnitude.

The combination of static and dynamic methods for the generation of high degrees of hydrogen compression allows us to reach pressures which are close to the conditions in giant planets [3]. In this experiment, results of reflectivity measurements show that molecular hydrogen as well as deuterium becomes conductive. On the basis of the simple estimates, like those used in Ref. [2], it is concluded that the increase of reflectance up to 10% corresponds to the ionization degree of 1% and to the boundary between insulating and conductive fluid hydrogen.

Much attention is also paid to the study of dense helium [4] due to the research of the atmosphere of white dwarfs. The quantum-mechanical approach with the linear response theory and the Kubo-Greenwood formalism [13,14] are used for calculation of reflectivity and conductivity [4]. The calculated dependence of the reflectance on temperature [4] is in a good agreement with experimental data [5]. However, the calculated dependence of the conductivity on the density [5] in fluid helium differs from the experimental one by 1–3 orders of magnitude. A sharp increase of the reflectance [5] indicates the onset of the conductive fluid helium. The estimated value of the density is 1.5 g/cm^3 at temperature about 3 eV. However, this value of the density is an ambiguous one. Another expression in Ref. [6] for the dependence of the band gap on the density gives value 10 g/cm^3, which is much higher than that obtained in Ref. [5]. The Drude model is used in Refs. [5,6] for the description of the optical properties of fluid helium.

The modeling of the helium and hydrogen demixing under the conditions encountered in giant planets is performed within the framework of the quantum molecular dynamics approach [7]. The jump is considered in the dependence of reflectivity on the demixing time as a distinctive signature of the liquid-liquid phase transition. The Kubo-Greenwood formula is used for the reflectivity calculation.

The nuclei are considered as classical particles in all the above-mentioned quantum-mechanical calculations. However, the quantum nature of nuclei makes significant impact on the properties of light elements, such as hydrogen and helium. As it is shown [8], taking into account this effect dramatically shifts the boundary between dielectric and conductive fluid hydrogen. Optical properties are also calculated in Ref. [8] within the Kubo-Greenwood formalism.

The dependence of reflectivity on density in Ge-doped plastics observed in the experiment [9] shows that the samples can be described as poor metals. The Drude-Sommerfeld pure metallic model of electrons does not give an adequate explanation of the results obtained. However, the Drude model gives a pretty good agreement with the experiment if the semiconductor description of the electrons [10,15,16] is used.

Shocked xenon plasma is considered in the present work. The reflectance of the shock-compressed xenon is measured in the unique experiments of Mintsev and Zaporoghets [17–20] for three values of the wavelength $\lambda = 1064$, 694, and 532 nm. The main goal of these experiments is an attempt to estimate both the free-charge-carrier concentration and the plasma frequency from the measured dependence of reflectivity on the plasma density. It is suggested in Ref. [17] that the profile of the dependence is similar to the case of collisionless plasmas. In this case, the dependence of the dielectric function (DF) on frequency is given by the formula $\varepsilon(\omega) = 1 - \omega_p^2/\omega^2$. And if $\omega_p > \omega$, it leads to the total internal reflection and the reflectivity is $R = 1$.

The dependencies of shocked xenon reflectivity on charge density n_e are given in Fig. 1 at the wavelength $\lambda = 694$ nm. The solid black line corresponds to the case of the collisionless plasma with the cutoff at the plasma frequency. The experimental data [18] are depicted by red stars at the values of n_e estimated in Ref. [18] using the chemical model [21]. However,

*saitovilnur@gmail.com

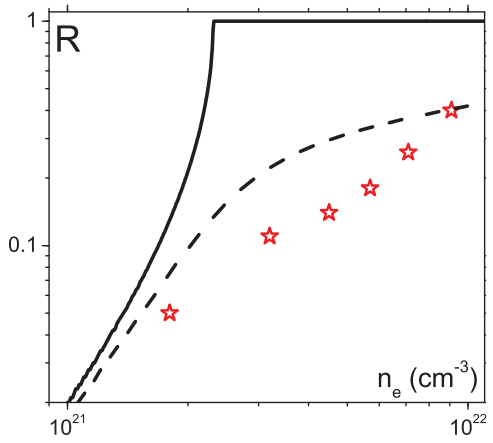

FIG. 1. (Color online) Dependence of reflectivity R on the electron concentration n_e at $\lambda = 694$ nm. The solid line corresponds to the case of collisionless plasma, where there is a cutoff of reflectivity at the plasma frequency. The red stars are the experimental data [18]. The dashed black line corresponds to the reflectivities calculated by the Drude formula with the static collisional frequency [22].

the measured dependence of the reflectance on the plasma density does not show a cutoff at the plasma frequency. The reflectance increases slowly with the increase of the plasma density.

The attempt to take into account the static collisional frequency within the framework of the Drude model [22] (the dashed line in Fig. 1) does not also give a satisfactory explanation of the results obtained. The more accurate expressions for the dynamic collisional frequency in the Born approximation [22] do not improve agreement with the experiment. If a pseudopotential is used for the electron-ion interaction, which takes into account a structure factor and local field corrections [23], the discrepancy becomes larger [22].

Other attempts to explain experimental results within the framework of the Drude model are associated with an artificial broadening of the wavefront [22,24–26]. Despite a certain improvement of the agreement with the experiment, this approach does not allow us to establish one-to-one correspondence between the reflectance values and the free-charge concentration. Moreover, there is no independent experimental confirmation of the essential wavefront broadening needed.

The shocked xenon plasma is an example of a warm dense matter (WDM). Theoretical description of the WDM is a challenging one and requires an application of unconventional methods [27–30]. The density functional theory (DFT) approach [31] is one of the most effective *ab initio* methods for the WDM properties description. The fundamental nature of this approach allows us to apply it for the description of a wide range of phenomena. Calculations of the DF for various substances are performed in Refs. [4,6–8,32–38].

The method of quantum molecular dynamics is used by Desjarlais [34] within the framework of the finite temperature DFT [39]. Only $\lambda = 1064$ nm is considered. The Kubo-Greenwood formula [13,14] and the Kramers-Kronig transformation are used for the calculation of the DF. The artificial wavefront broadening is not applied. The results [34] are in a better agreement with the experimental data [17] in comparison with the reflectivities obtained via the Drude formula [22]. However, the results [34] are still significantly higher than the measured ones [17] at low densities. The band-gap corrections improve the agreement with the experiment at lower densities but underestimate reflectivities at high densities.

The DFT approach is used in this work as in Ref. [34]. However, a more accurate longitudinal expression is applied for the calculation of the imaginary part of the DF in contrast with Ref. [34]. The advantage of using the longitudinal expression instead of the Kubo-Greenwood formula is shown for the calculation of the imaginary part of the DF in Ref. [35] for various substances, such as Si, SiC, AlP, GaAs, and diamond. We do not introduce the wavefront broadening.

The basic expressions used for the calculation of the DF and reflectance are presented in the second section. The expressions for different components of the dielectric tensor are compared with each other. The calculation method is considered in the third section. The method is based on the DFT with the expressions for the DF from Sec. II. The method of calculation of the plasma frequency is developed in Sec. IV within the framework of the DFT; results of the calculation of the dependence of the plasma frequency on density are presented. The applicability of the "free electrons" concept is discussed in Sec. V; the dependence of the effective concentration of "free electrons" on the plasma density is calculated. In Sec. VI, the dependencies of reflectivity on density are calculated for all three wavelengths $\lambda = 1064, 694$, and 532 nm using the longitudinal expression for the DF within the framework of the DFT. The convergence and accuracy of the results obtained are analyzed as well. In Sec. VII, the results obtained are discussed and compared with [34]. The dependence of the reflectivity on density is calculated using the Kubo-Greenwood formula for the imaginary part of the DF for validation of the calculation method. Section VIII contains our conclusions.

II. BASIC EXPRESSIONS

The DFT is used for the calculation of the DF and reflectivity of shocked the xenon plasma. Forty-six core electrons of xenon atom are considered by means of the projector augmented wave (PAW) method potential [40], which is nonlocal. The Kohn-Sham set of equations with the PAW potential, which effectively takes into account core electrons, is solved for eight valent electrons.

There are two types of the electron-ion pseudopotentials and PAW potentials: local and nonlocal. Local potentials are diagonal in the coordinate representation and their matrix elements can be represented by the following expression:

$$\langle \mathbf{r}|\mathbf{V}|\mathbf{r}'\rangle = \mathbf{V}(\mathbf{r})\delta(\mathbf{r}-\mathbf{r}'). \quad (1)$$

Nonlocal potentials $V(\mathbf{r},\mathbf{r}')$ are not diagonal and their effect on a wave function $\psi(\mathbf{r}')$ can not be represented just as a product of $V(\mathbf{r},\mathbf{r}')$ and $\psi(\mathbf{r}')$. Therefore, we are to calculate the following integral:

$$\langle \mathbf{r}|\mathbf{V}|\psi\rangle = \int \mathbf{V}(\mathbf{r},\mathbf{r}')\psi(\mathbf{r}')\mathbf{d}^3\mathbf{r}'. \quad (2)$$

Since a nonlocal potential is an integral operator, it does not commute with the coordinate operator $\mathbf{r}$. This property imposes restrictions on the expressions for the DF calculation.

The DF is a complex function and can be expressed as $\varepsilon = \varepsilon^{(1)} + i \cdot \varepsilon^{(2)}$. Depending on the character of the external field, there are two expressions for the components of the DF tensor: a longitudinal expression [41–43] and a transverse one [13,14].

We consider the interaction of the electromagnetic (transverse) radiation with matter and therefore the response function is the transverse DF. The dependence on frequency ω of the imaginary part of the transverse DF is defined by the following expression in the long-wavelength limit:

$$\varepsilon_T^{(2)}(\omega,\mathbf{R_I}) = (4\pi^2 e^2/3\omega^2\Omega) \lim_{|\mathbf{q}|\to 0} \sum_{n,n',\alpha,\mathbf{k}} 2\mathrm{w}_\mathbf{k} \times [f(E_{n',\mathbf{k}+\mathbf{q}}) - f(E_{n,\mathbf{k}})] \cdot |\langle\psi_{n'\mathbf{k}}|\hat{\mathbf{v}}_\alpha|\psi_{n\mathbf{k}}\rangle|^2 \times \delta(E_{n',\mathbf{k}+\mathbf{q}} - E_{n\mathbf{k}} - \hbar\omega) \quad (3)$$

at a given ion configuration $\mathbf{R_I}$ and temperature T, where e is the elementary charge, Ω is a system volume, $\mathbf{q}$ is a wave vector of the incident radiation, and $\hbar$ is the Plank constant.

The summation is carried out over all electron states n, n'. The contribution of the sum terms with $n = n'$ (intraband transitions) are taken into account as well as the contribution of the terms with $n \neq n'$ (interband transitions).

The summation over index α multiplied by 1/3 stands for the averaging over three spatial coordinates. This assumes isotropy of the considered system, which is justified for the case of a plasma. The summation is also carried out over all $\mathbf{k}$ points in the Brillouin zone, taking into account the weights $\mathrm{w}_\mathbf{k}$ of the $\mathbf{k}$ points. The factor 2 before the weights allows for the electron spin degeneracy. $f(T,E_{n,\mathbf{k}})$ is the Fermi-Dirac distribution function at temperature T, which defines an occupation of a state n. $E_{n,\mathbf{k}}$ is an eigenvalue (an energy level) corresponding to the wave function $\psi_{n,\mathbf{k}}$. $\psi_{n,\mathbf{k}}$ is a solution of the Kohn-Sham equation. We find this solution as a sum of plane waves and therefore it can be represented by means of the Bloch function $\psi_{n,\mathbf{k}} = e^{i\mathbf{kr}} \cdot u_{n,\mathbf{k}}$, where $u_{n,\mathbf{k}}$ is a cell periodic part. $\hat{\mathbf{v}}$ is the velocity operator, which can be expressed by the commutator

$$\hat{\mathbf{v}} = d\mathbf{r}/dt = (i/\hbar)[H,\mathbf{r}]. \quad (4)$$

If the potential in the Hamiltonian H is local, the expression (4) gives $\hat{\mathbf{v}} = \mathbf{p}/m$, where $\mathbf{p}$ is the momentum operator and m is the electron mass. Substituting this results in Eq. (3), we obtain the Kubo-Greenwood formula [13,14]

$$\varepsilon_T^{(2)}(\omega,\mathbf{R_I}) = (4\pi^2 e^2\hbar^2/3m^2\omega^2\Omega) \lim_{|\mathbf{q}|\to 0} \sum_{n,n',\alpha,\mathbf{k}} 2\mathrm{w}_\mathbf{k} \times [f(T,E_{n',\mathbf{k}+\mathbf{q}}) - f(T,E_{n,\mathbf{k}})] |\langle u_{n',\mathbf{k}}|\nabla_\alpha - i\mathbf{k}_\alpha|u_{n,\mathbf{k}}\rangle|^2 \delta(E_{n',\mathbf{k}+\mathbf{q}} - E_{n,\mathbf{k}} - \hbar\omega). \quad (5)$$

However, this substitution is incorrect for the nonlocal potentials. Since the potential does not commute with the coordinate operator, the additional term arises in the commutator (4) [44]:

$$\hat{\mathbf{v}} = \mathbf{p}/m + (i/\hbar)[V(\mathbf{r},\mathbf{r}'),\mathbf{r}]. \quad (6)$$

Consequently, the Kubo-Greenwood formula is incorrect for the nonlocal potentials.

Despite the isotropy of the system considered, its responses depend on the nature of the perturbation (longitudinal or transverse) and, generally, do not coincide with each other. The simplest example of this statement is the conductivity tensor obtained within the framework of the hydrodynamic model of plasmas. However, the longitudinal and transverse DF are equal to each other in the long-wavelength limit. In this limit the velocity operator can be expressed as [45]

$$\hat{\mathbf{v}} = \lim_{|\mathbf{q}|\to 0} [H, \exp(i\mathbf{qr})]/\hbar|\mathbf{q}|. \quad (7)$$

The substitution of (7) in Eq. (3) gives the expression for the imaginary part of the longitudinal DF,

$$\varepsilon_L^{(2)}(\omega,\mathbf{R_I}) = (4\pi^2 e^2/3\Omega) \lim_{|\mathbf{q}|\to 0} \frac{1}{|\mathbf{q}|^2} \sum_{n,n',\alpha,\mathbf{k}} 2w_\mathbf{k} [f(T,E_{n',\mathbf{k}+\mathbf{q}}) - f(T,E_{n,\mathbf{k}})] |\langle u_{n',\mathbf{k}+\mathbf{e}_\alpha q} \mid u_{n,\mathbf{k}}\rangle|^2 \times \delta(E_{n',\mathbf{k}+\mathbf{q}} - E_{n,\mathbf{k}} - \hbar\omega), \quad (8)$$

where the unit vector $\mathbf{e}_\alpha$ determines the direction of the Cartesian axis corresponding to the coordinate α. The expression (8) is obtained in Refs. [41–43] within the framework of the first-order perturbation theory approach and the random-phase approximation (RPA). Since we use the conversion of the velocity operator for the derivation of (8), the longitudinal expression has no disadvantages, which the Kubo-Greenwood formula (5) has. The formula (8) can be used for any electron-ion potentials. The Kubo-Greenwood formula can be used only with corrections, which take into account nonlocality of a PAW potential [46].

The expression (5) can be derived for the local potentials from (8) by applying the substitution

$$\lim_{|\mathbf{q}|\to 0} \frac{\langle u_{n\mathbf{k}}|u_{n'\mathbf{k}+\mathbf{q}}\rangle}{|\mathbf{q}|} = -\frac{\hbar^2}{m} \lim_{|\mathbf{q}|\to 0} \frac{\langle u_{n'\mathbf{k}}|(\nabla - i\mathbf{k})|u_{n\mathbf{k}}\rangle}{E_{n'\mathbf{k}+\mathbf{q}} - E_{n\mathbf{k}}}. \quad (9)$$

The real part of the DF is obtained by the Kramers-Kronig transformation

$$\varepsilon^{(1)}(\omega,\mathbf{R_I}) = 1 + \frac{2}{\pi} P \int_0^\infty d\omega' \frac{\omega'\varepsilon^{(2)}(\omega',\mathbf{R_I})}{(\omega')^2 - (\omega - i\eta)^2}, \quad (10)$$

where P denotes the principle value (in the limit $\eta \to 0$).

The response function of the system with respect to an external perturbation is not the DF but the inverse DF in the general case. Due to the casuality principle, the Kramers-Kronig transformations are always true for the inverse DF. Therefore, the expression (10) is valid for the DF only in the long-wavelength limit [47].

The expressions (3), (5), and (7)–(9) for the imaginary part of the DF are also derived in the long-wavelength limit. This limit holds in the context of this study both from the experimental point of view and from the point of view of the *ab initio* calculation method.

Considering the experimental conditions, we should compare the field penetration depth $d = \lambda/(4\pi n_2)$ [48,49] with the wavelength of the incident radiation in the medium $\lambda' = \lambda/n_1$, where n_1 and n_2 are real and imaginary parts of the refraction coefficient. $d/\lambda' \ll 1$ for the xenon plasma densities considered in this work.

The characteristic size of the system is the length of the computational cell L in the DFT model (see Sec. III). The ratio $L/\lambda' \ll 1$ is valid for our case as well.

The values of the DF are calculated for the fixed ionic configurations. The resulting value of the DF is calculated for the given temperature and density by averaging over the entire ensemble of M ionic configurations,

$$\varepsilon^{1,2}_{L,T}(\omega) = \frac{1}{M}\sum_{I=1}^{M} \varepsilon^{1,2}_{L,T}(\omega, \mathbf{R_I}). \tag{11}$$

The averaged DF is substituted in the Fresnel formula for the calculation of the reflectivity

$$R = \left|\frac{(\sqrt{\varepsilon}-1)}{(\sqrt{\varepsilon}+1)}\right|^2. \tag{12}$$

III. CALCULATION METHOD

The Vienna *Ab initio* Simulation Package (VASP) [50–53] plane-wave code is used for the DFT modeling in this work. The longitudinal expression (8) is applied. The generalized gradient approximation (GGA) for the exchange and correlation part of the density functional is used. The type of the functional is Perdew-Burke-Ernzerhof (PBE) [54]. The solution of the Kohn-Sham equations for the wave functions and corresponding energy levels is used for the calculation of the DF components in Eq. (8). The energy cutoff of the plane waves basis set is 180 eV.

The finite simulation volume leads to a discrete spectrum of the eigenvalues. The Gaussian function is used as an approximation of the δ function in the expressions (8) and (5). The Gaussian width coincides with the electron temperature (the parameter of the Fermi-Dirac distribution function) in the current version of VASP. However, this approximation for the width is valid only for the case of low temperatures and it underestimates the values of the DF and reflectivity in the case of plasmas, where electron temperatures are several eV. It means that if the Gaussian is too broadened, the approximation of the δ function becomes worse.

The Gaussian width is chosen to be equal to 0.03 eV in this work. The DF is also calculated for the Gaussian widths from 0.01 to 0.1 eV and the results are not changed in this range. If the Gaussian width is too small, it leads to nonphysical peaks in $\varepsilon^{(2)}(\omega)$.

Calculations are performed in the canonical ensemble. The ion temperature is controlled by the Nosé-Hoover thermostat [55,56]. The electron temperature coincides with the ion temperature and is established by the Fermi-Dirac distribution for occupancies $f(T,E)$. The temperature of the system considered is $T \sim 30\,000$ K. The values of temperature and plasma density, which correspond to the experiments [17–20], are given in Table I.

The DF values are averaged over the set of ion configurations (11). These configurations are obtained within the framework of the quantum molecular dynamics [57]. The forces acting on ions are evaluated via the Hellmann-Feynman theorem. Then the classical Newtonian equations of motion are integrated to obtain trajectories of particles. Depending on the particle density in the computational cell, the trajectories have 4000–10 000 steps with the time step 2 fs. From 5 to 10 statistically independent [58] configurations are chosen for averaging.

TABLE I. Densities ρ and temperatures T [17–20].

$\lambda = 1064$ nm		$\lambda = 694$ nm, 532 nm	
ρ, g/cm^3	T, K	ρ, g/cm^3	T, K
0.51	30050	0.53	32900
0.97	29570	1.1	33100
1.46	30260	1.6	33120
1.98	29810	2.2	32090
2.7	29250	2.8	32020
3.84	28810	3.4	31040

The range of plasma densities studied is $\rho = 0.51$–3.84 g/cm^3. The number of particles in the computational cell varies from 16 at the lowest densities up to 128 at the highest density. The periodic boundary conditions are used. The increase of the density leads to the decrease of the calculation time at the fixed number of particles in the computational cell.

IV. PLASMA FREQUENCY

Two methods of the plasma frequency evaluation are suggested in the present paper. The first one is based on the calculation of the real part of the dynamic conductivity $\sigma(\omega)$. It is associated with the imaginary part of the DF by the relation $\sigma(\omega) = \varepsilon_0\omega\varepsilon^{(2)}(\omega)$, where ε_0 is the dielectric constant. The obtained dependence $\sigma(\omega)$ can be fitted at low frequencies by the Drude formula [11,12],

$$\sigma(\omega) = \left(\varepsilon_0\omega_p^2\tau\right)/(1+\omega^2\tau^2). \tag{13}$$

The parameters of the approximation are the relaxation time τ and the plasma frequency ω_p, which we are looking for. This method is also used in Refs. [46,59].

The second method is based on the sum rule [60]:

$$\int_0^\infty \omega\varepsilon^{(2)}(\omega)d\omega = \frac{\pi}{2}\omega_p^2, \tag{14}$$

where all the electrons are considered as free in the definition of ω_p. The DFT approach does not separate valent electrons into bound and free ones. Due to the necessity to calculate integral (14) numerically, we consider the following function, which depends on the upper limit $\omega_{\max}$:

$$S(\omega_{\max}) = \frac{2m\varepsilon_0}{\pi n N_v e^2}\int_0^{\omega_{\max}} \varepsilon^{(2)}(\omega)\omega d\omega, \tag{15}$$

where we substitute $nN_ve^2/m\varepsilon_0$ into (14) instead of ω_p^2. The number of valent electrons is $N_v = 8$ for xenon in the DFT framework, and n is the total concentration of ions and atoms.

The functions $S(\omega_{\max})$ are shown in Fig. 2 for the range of xenon densities from $\rho = 0.53$ g/cm^3 to 3.4 g/cm^3. As one can see, the function $S(\omega_{\max})$ has two limiting values with nearly zero slopes. We denote them as S_1 and S_2. The value $S_2 = 1$ corresponds to eight electrons. This fact indicates to the correctness of the results obtained.

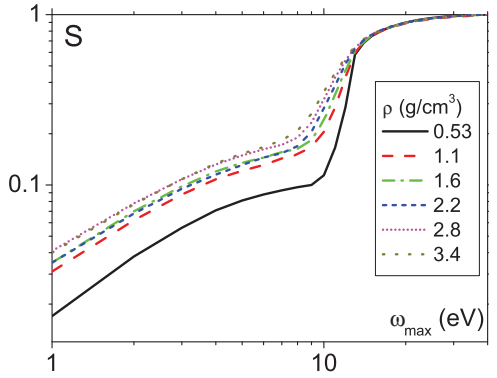

FIG. 2. (Color online) Dependencies of function S on the upper limit $\omega_{\max}$ at various densities ρ.

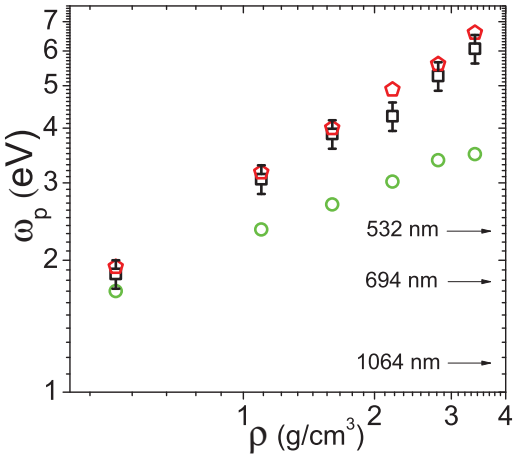

FIG. 3. (Color online) Dependencies of plasma frequency on density of xenon plasma. Pentagons correspond to values of ω_p calculated by using Drude formula (13). Squares are results calculated with formula (16). Circles are estimates of plasma frequencies obtained in Refs. [18,22]. Arrows indicate the values of the frequencies, which correspond to the wavelengths 1064, 694, and 532 nm.

The value S_1 at $\omega_{\max}$ about 10 eV can be related to the plasma frequency. In fact, all the possible transitions between the electron states are taken into account within the DFT framework in the expression (8) for the imaginary part of the DF included in Eq. (15). These transitions can be divided into interband and intraband transitions. The interband transitions correspond in plasma to the transitions between bound states with different principle quantum numbers (spectral lines) and to the transitions between bound and free states (photoionization). The intraband transitions correspond in plasma to the transitions in the continuous spectrum (free-free transitions) and to the transitions between bound states with equal principle quantum numbers but with different orbital quantum numbers.

The plasma frequency is defined by the intraband transitions in the continuous spectrum. The first limiting value S_1 of the function $S(\omega_{\max})$ is a contribution of low-frequency transitions or intraband transitions. Thus, the limiting value S_1 can be applied for the calculation of ω_p,

$$\omega_p^2 = (nN_v e^2/m\varepsilon_0)S_1. \tag{16}$$

It should be noted that the values of the plasma frequency ω_p obtained in this way may be slightly overestimated due to inclusion of the intraband transitions in the discrete spectrum. However, analysis of the electron density of states reveals that the possible contribution of these transitions is vanishingly small in the given range of the shocked xenon plasma parameters.

The dependencies of ω_p on density calculated by each of two methods are shown in Fig. 3. The dependencies obtained by the Drude formula (13) within the framework of the free electron model and those calculated with the formula (16) almost coincide with each other. This fact can be considered as a confirmation that the first limiting value of $S(\omega_{\max})$ is responsible for the contribution of the transitions in the continuous spectrum.

The values of plasma frequency obtained in this work are close to the estimations [18,22] only at low densities. There is an increasing discrepancy of ω_p values with the increase of density.

The imaginary part of the DF is included in the expressions for both the reflectivity (12) and the plasma frequency (16). One and the same sum over states defines explicitly both values. Therefore, the values of the plasma frequency calculated within the framework of the approach used in this work are directly associated with the dependencies of the reflectivity on the plasma density.

V. FREE ELECTRONS

Low-temperature plasma is considered at low densities as consisting of electrons, ions, and atoms. Atoms are distributed over ground and excited states. Electrons are divided into bound and free. Bound electrons form a discrete spectrum of the atomic energy levels. Free electrons have a continuous spectrum. This conventional picture fails with increase of the plasma density.

Excited levels broaden due to the Stark effect and upper levels merge, forming a quasicontinuous spectrum. Its lower border is defined by the formulas of the Inglis-Teller type.

Another restriction of the pair excited states occurs, since their lifetime decreases with the increase of the principal quantum number due to Coulomb collisions. The lifetime becomes zero at energies below ionization limit by a certain amount ΔE. Electron and ion states in the range of ΔE can be attributed to quasicontinuous collective many-body states of a fluctuation nature [61–63].

The Inglis-Teller lowering as well as ΔE increase with the increase of the concentration of charges. Therefore, the selection of the free states in the spectrum of electron states becomes more and more arbitrary and approximate with the increase of the plasma density.

Moreover, the free electron number density is not an observable value in quantum mechanics. However, one can introduce an effective concentration of free-charge carriers n_e, using the values of the plasma frequency from Sec. IV and the formula which is valid for ideal plasmas,

$$\omega_p^2 = n_e e^2/\varepsilon_0 m_e. \tag{17}$$

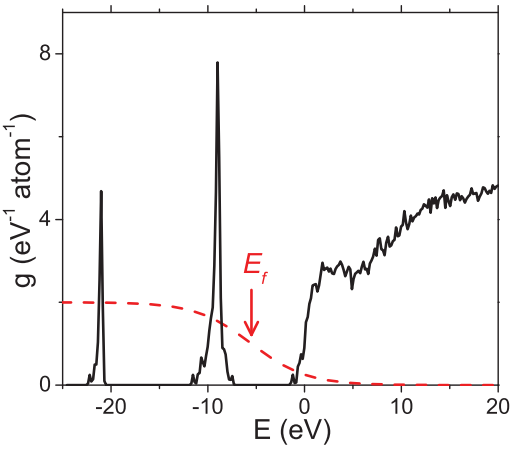

FIG. 4. (Color online) An example of the electron density of states at $\rho = 1.6$ g/cm^3.

In particular, it follows from (16)

$$n_e = S_1 n N_v. \tag{18}$$

In addition to two methods mentioned in Sec. IV, one can estimate n_e considering the states with energies greater than the Fermi energy E_f as free electron states. Thus, the concentration of free-charge carriers n_e can be calculated with the formula

$$n_e/n = 2\int_{E_f}^{\infty} f(T,E)g(E)dE, \tag{19}$$

where $g(E)$ is the electron density of states that depends mostly on the plasma density according to Refs. [6,61]. An example of the characteristic shape of $g(E)$ for $\rho = 1.6$ g/cm^3 is shown in Fig. 4.

The values of n_e at different densities ρ are given for the four approaches in Table II. The values of n_e calculated with the formulas (13) and (17) are given in the second column. The third column comprises the most reliable calculation results using the formulas (16) and (17). The values of the effective free-electron concentrations calculated with the formula (19) are given in the fourth column. The values in all three columns are in a satisfactory agreement with each other.

The estimates of n_e obtained in Refs. [18,22] are given in the fifth column. The concentrations of free electrons and the corresponding values of the plasma frequency in Refs. [18,22] are obtained within the chemical plasma model [21]. The Saha

TABLE II. Effective concentrations of free electrons n_e at various plasma densities ρ.

	$n_e \times 10^{-21}$, cm^{-3}			
ρ, g/cm^3	(13) and (17)	(16) and (17)	(19)	[18,22]
0.53	2.7	2.5	4	2.1
1.1	7.3	6.8	8.2	4
1.6	11.6	11	12	5.2
2.2	17.4	13	16.4	6.6
2.8	23	20	20	7.8
3.4	31.6	26.7	25.4	8.8

equation is used. The effects of the Coulomb attraction and short-range repulsion are taken into account in the form of the Debye correction and the approximation of hard spheres [64], respectively. The discrepancy between the results [18,22] and the figures in the second, third, and fourth columns indicates the uncertainty of the chemical model for dense plasmas. The discrepancy increases with the increase of the plasma density.

It should be emphasized that the estimates [18,22] of n_e and ω_p are connected by the formula (17) and are related only to the parameters of the plasma produced by shock compression of xenon. The estimates [18,22] of n_e and ω_p are not connected with the dependence of the reflectivity on the plasma density, which is also measured in Refs. [17–20]. Contrary to Refs. [18,22], the approach developed in this paper gives the self-consistent determination of both ω_p and n_e and reflectivity.

Note that these methods of the estimation of the effective free electron concentration can be used not only for monatomic substances like xenon but also for mixtures [32,33]. Two other approaches for the estimation of the effective free-electron density have been proposed recently for WDM. One is based on the accurate analysis of the electron density of states [65] and the other is based on the free-electron pressure analysis [66].

VI. REFLECTIVITY

A. Calculations results

The measured and calculated values of the reflectivity dependence on density are shown in Fig. 5 for the wavelengths of laser radiation 1064, 694, and 532 nm. The experimental data [17–20] are depicted by stars. The squares correspond to calculation results obtained in this work.

As one can see, the calculated reflectivities for the wavelengths 1064 and 694 nm are in a good agreement with the experimental data both in the absolute values and in the density dependence in the range of $\rho \geqslant 1$ g/cm^3. The only point drops out at the low density $\rho = 0.5$ g/cm^3. This divergence at low density can be associated in particular with the fact that the ratio of the penetration depth and the wavelength in the medium becomes $d/\lambda' \sim 0.3$ at $\rho = 0.5$ g/cm^3. Therefore, our DFT approach has a limited applicability at low densities. The parameter $d/\lambda' < 0.1$ at high densities. It ensures the applicability of this approach in the range $\rho > 1$ g/cm^3. In addition, the computational applicability of the DFT becomes less reliable with the decrease of the density.

The ratio is $d/\lambda' = 0.16$ for the wavelength 532 nm at $\rho = 1$ g/cm^3. Thus, unlike the case of the wavelengths of 1064 and 694 nm, the applicability of the long-wavelength approximation for 532 nm is also restricted for a given density. The ratio $d/\lambda' < 0.1$ for larger ρ as well as for 1064 and 694 nm. Theoretical values of the reflectivity at 532 nm are overestimated in comparison with the experimental ones. However, the relative dependence of the reflection coefficient on the density is reproduced.

The arrows indicate in Fig. 5 the densities where the frequency of the incident radiation coincides with the plasma frequency calculated in Sec. IV. Thus, the calculation shows

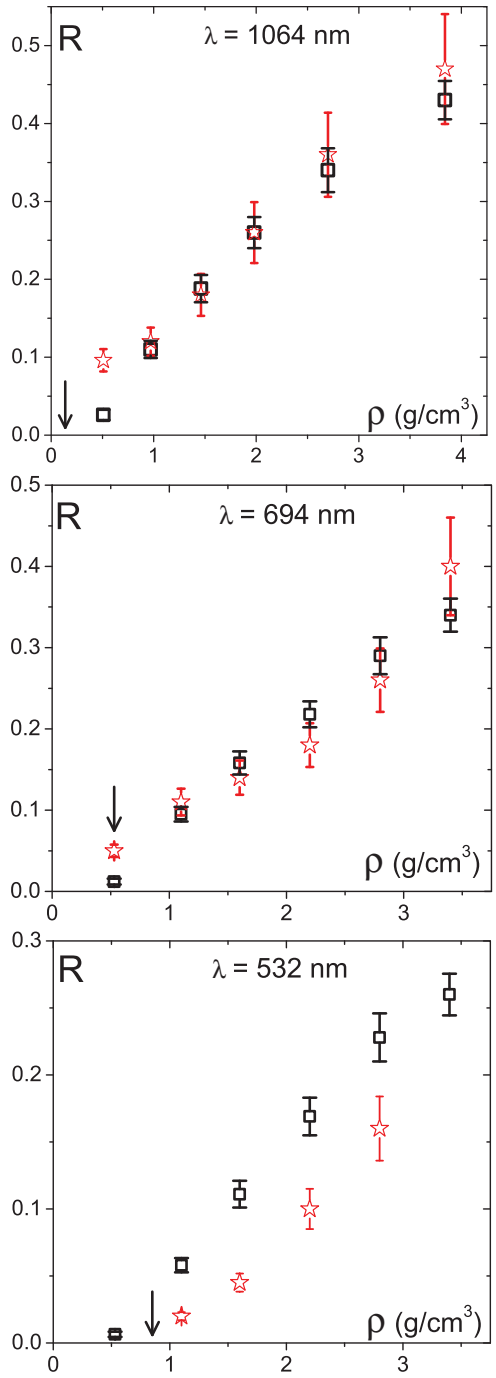

FIG. 5. (Color online) Dependencies of the shocked xenon plasma reflectivity on the plasma density at various values of wavelengths. The experimental data [17–20] are depicted by stars. The squares correspond to the calculation data. The arrows indicate the values of the plasma density where the frequency of incident radiation and the plasma frequency coincide with each other.

that there is no cutoff at the plasma frequency. It solves the problem which is shown in the Introduction.

B. Accuracy of the results

The convergence of the results obtained are analyzed over four parameters of the calculation: the upper limit of integration in Eq. (10), the number of particles in the computational cell, the number of **k** points in the Brillouin zone, and the number of configurations of the ions used for averaging. The analysis of the dependence of reflectivity on the upper limit of the integral (10) shows that the value $\omega_{\max} = 40$ eV is sufficient for the convergence.

The analysis of the dependence of the reflectivity on the number of particles N shows that the results depend weakly on N at the low plasma density and the number of particles $N = 16$ is sufficient. The increase of N leads to a considerable increase in the calculation time. Therefore, it is important to determine the minimum amount of particles in the unit cell where the convergence is achieved, especially for the low plasma densities. It means that it is necessary to increase the computational cell with the increase of the plasma density. For the high plasma densities, the calculations are performed for 64 particles. Calculations for 128 particles are also performed to check the convergence of the results.

The calculated reflectivity values (Fig. 5) are obtained for one Γ point in the Brillouin zone. The values of reflectivity are calculated for different numbers of **k** points from 1 to 64 to check the convergence of the results. The analysis of the results shows that an increase of **k** points does not affect the value of the reflection coefficient at temperatures about 3 eV considered.

The DF values for a given density are averaged over the number of the statistically independent configurations [58]. The averaging determines the value of the relative error of the DF. The number of configurations is not less than 5. The error of reflectivity is determined by the standard relation

$$\Delta R = \sqrt{\left(\frac{\partial R}{\partial \varepsilon^{(1)}}\Delta\varepsilon^{(1)}\right)^2 + \left(\frac{\partial R}{\partial \varepsilon^{(2)}}\Delta\varepsilon^{(2)}\right)^2}. \qquad (20)$$

The error $\Delta\varepsilon^{(2)}$ of the imaginary part of the DF is the standard deviation of $\varepsilon^{(2)}$ for the case of the averaging over statistically independent configurations. The increase of the number of the configurations leads to the decrease of $\Delta\varepsilon^{(2)}$. It is assumed that the relative error $\Delta\varepsilon^{(2)}/\varepsilon^{(2)}$ does not depend on frequency.

The errors of the the real $\Delta\varepsilon^{(1)}$ and imaginary $\Delta\varepsilon^{(2)}$ parts of the DF are connected by the following expression

$$\Delta\varepsilon^{(1)}(\omega) = \frac{2}{\pi} P \int_0^\infty \frac{\Delta\varepsilon^{(2)}(\omega')\omega'}{\omega'^2 - \omega^2} d\omega'. \qquad (21)$$

At the lowest plasma density, the relative error of the imaginary part of the DF is the largest but it does not exceed 15%. The relative error $\Delta\varepsilon^{(1)}/\varepsilon^{(1)}$ is about 1,5% and the ratio of derivatives is $(\partial R/\partial\varepsilon^{(1)})/(\partial R/\partial\varepsilon^{(2)}) \ll 1$ at the least value of ρ. Thus, at the lowest plasma density the imaginary part of the DF makes a decisive contribution to the reflectivity error, which equals 30% in this case.

While increasing the plasma density up to $\rho = 3.84$ g/cm^3, the derivatives of the reflectance with respect to the components of the DF become equal to each other as well as the relative errors $\varepsilon^{(1)}$ and $\varepsilon^{(2)}$. Thus, the real and imaginary parts of the DF contribute equally to ΔR. The absolute value of ΔR increases, but the relative error decreases significantly to less than 5%. Therefore, it is not necessary to increase the accuracy of the imaginary part of the DF for the large values of the plasma density.

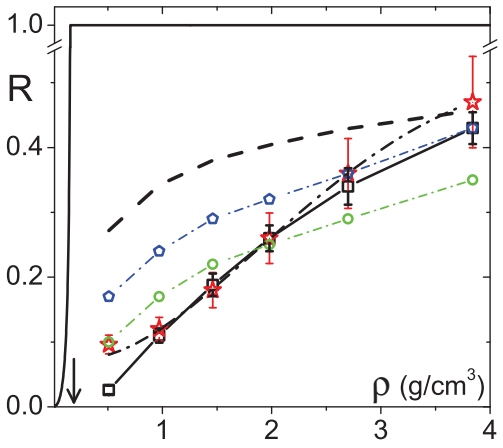

FIG. 6. (Color online) Dependencies of the reflectivity on the plasma density at the wavelength 1064 nm. The solid line is the case of collisionless plasma. The dashed line corresponds to the reflectivities calculated by the Drude formula with the static collisional frequency [22]. The dash-dot line is the Drude model with a wide wave front as a fitting parameter [22,24–26]. The stars are the experimental data [17]. The pentagons connected by the dashed line are results or Ref. [34]; the circles connected by the dashed line are results of Ref. [34] with band-gap corrections; the squares connected by the solid line are the results of this work. The arrows indicate the plasma density where the frequency of the incident radiation equals to the plasma frequency.

VII. DISCUSSION

The dependence on the plasma density of the reflectivity for the laser radiation at the wavelength 1064 nm is shown in Fig. 6. Different theoretical approximations are grouped together with the experimental data [17] presented by stars. The solid line corresponds to the case of a collisionless plasma with a cutoff at the plasma frequency. The dashed line corresponds to reflectivities calculated by the Drude formula with the static collisional frequency [22]. These lines and points are similar to those shown in Fig. 1. According to the experimental data, one can see that there is no cutoff at the plasma frequency. Also, using the Drude formula with a nonzero collision frequency can not explain the experimental data.

In the papers [22,24–26], it is assumed that the density in the shock-compressed xenon increases not abruptly but there is a region of finite width, in which the density increases smoothly to a final value. Thus, the wavefront has a finite width and the laser light is reflected not directly from the xenon plasma, but from the extended front. The assumption, that the wavefront width is about 1 μm, improves significantly the agreement with the experiment in comparison with the assumption of a sharp front, when the Drude formula is used. However, the effect of the front broadening has no independent experimental support. In this paper, we do not consider the effect of the wavefront broadening, which can still make a contribution to the reflectivity of the shock-compressed xenon plasma, although in a much lesser degree than expected in Refs. [22,24–26].

As mentioned in the Introduction, the DFT approach for the calculation of the shocked xenon plasma reflectivity is introduced in Ref. [34] without using the hypothesis of the front broadening. The pentagons connected by the dashed line in Fig. 6 correspond to the calculation results [34]. As one can see, the results [34] are in a much better agreement with the experiment in comparison with the Drude formula. However, there is also a noticeable discrepancy with the experiment at the low plasma densities.

An assumption about an increase of the energy gap between free and bound states is introduced in Ref. [34] to improve the agreement with the experiment [17]. The assumption is analogous to that used to correct the underestimation of the band gap in the semiconductor spectra. The effect is observed in the calculation of the electron density of states within the framework of the DFT. As shown in Ref. [45], these corrections are introduced in the expression for the imaginary part of the DF,

$$\varepsilon^{(2)}_{\mathrm{gap}}(\omega) = \left[\frac{\hbar\omega}{\hbar\omega - \Delta}\right]^2 \varepsilon^{(2)}(\omega), \tag{22}$$

where Δ is the magnitude of the correction, which increases the gap between the bound and free electron states. The correction (22) allows for the contributions in the DF and reflectivity, which are not included within the RPA.

The gap is increased by the value $\Delta = 2.5$ eV in Ref. [34]. The results of the calculation of the reflectivity with the band-gap corrections are shown in Fig. 6 by the circles connected by the dashed line. It improves the agreement of the calculation results with the experiment at the low densities, but it leads to the underestimation of the reflection coefficient at the high densities. The dependencies of the reflectivity on the plasma density [34] with and without corrections are almost parallel. Thus, the introduction of these amendments affects only the absolute values and does not affect the character of the dependence of the reflectivity on the plasma density.

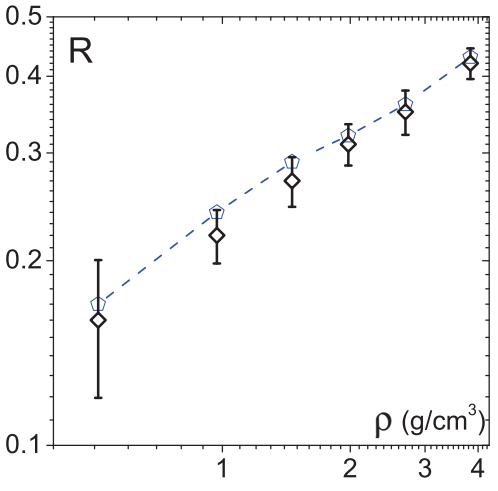

FIG. 7. (Color online) Reflectivities calculated in the DFT framework with the Kubo-Greenwood formula at various densities: The pentagons connected by the dashed line are the results of Ref. [34], and the diamond are results of this work.

The discussion performed reveals the importance of the density of states for the reflectivity determination. Therefore, we can return to the discussion of Fig. 4, where there is a gap between continuous states ($E - E_f > 0$) and the discrete level at $E \approx -10$ eV. However, the idea of the electron spectrum in dense plasmas as a combination of the continuous spectrum of free states and the discrete spectrum of bound electrons separated by an energy gap is not quite correct [62] as discussed in Sec. V. Thus, the validity of the amendments introduced in Ref. [34] requires further analysis and elaboration in the case of calculations of the WDM properties.

The calculation results obtained in this paper are in a better agreement with the experiment in comparison with Ref. [34] both in the absolute values and in the density dependence *without* the introduction of any amendments to either the shockwave front width or the band gap. The rate of the reflectivity increase with the plasma density increase obtained in this study is considerably higher compared to Ref. [34].

As previously mentioned, the main difference of the approach developed in the present work from Ref. [34] is the application of the longitudinal expression (8) instead of the transverse Kubo-Greenwood expression (5). We reproduce the calculations of Ref. [34] in order to check this conclusion. As one can see in Fig. 7, our values are in a good agreement with the data [34], despite the fact that the earlier version of the PBE exchange and correlational functional [67] is used in Ref. [34]. We calculate also the reflectivity with different PAW models included in VASP, and no effect is found. Therefore, the use of the longitudinal expression (8) instead of the Kubo-Greenwood formula (5) is the main reason of the better agreement of our DFT results with the experimental data.

VIII. CONCLUSIONS

The dependence of the shock-compressed xenon plasma reflectivity on the plasma density is calculated for different wavelengths within the framework of the DFT.

The expression for the longitudinal component of the dielectric function gives a significantly better agreement with the experiment in comparison with the Drude model with the collision frequency in the Born approximation as well as with the DFT approach using the Kubo-Greenwood formula. The long-wavelength limit is considered.

The method of the plasma frequency calculation is developed based on the sum rule within the DFT approach. The approach gives the self-consistent determination of both plasma frequency and the reflectivity dependence on density.

ACKNOWLEDGMENTS

The authors thank V. B. Mintsev and Yu. B. Zaporozhets for the information about the results of the measurements and M. P. Desjarlais for the useful criticism of Refs. [68,69]. The calculations are carried out on the computing clusters MVS-100K of the Joint Supercomputer Center RAS and K-100 of the Keldysh Institute of Applied Mathematitcs RAS. This work was supported by Grant No. 14-19-01295 of the Russian Science Foundation.

[1] G. W. Collins, P. M. Celliers, D. M. Gold, L. B. da Silva, and R. Cauble, Contrib. Plasma Phys. **39**, 13 (1999).
[2] P. M. Celliers, G. W. Collins, L. B. Da Silva, D. M. Gold, R. Cauble, R. J. Wallace, M. E. Foord, and B. A. Hammel, Phys. Rev. Lett. **84**, 5564 (2000).
[3] P. Loubeyre, P. M. Celliers, D. G. Hicks, E. Henry, A. Dewaele, J. Pasley, J. Eggert, M. Koenig, F. Occelli, K. M. Lee, R. Jeanloz, D. Neely, A. Benuzzi-Mounaix, D. Bradley, M. Bastea, S. Moon, and G. W. Collins, High Pressure Res. **24**, 25 (2004).
[4] P. M. Kowalski, S. Mazevet, D. Saumon, and M. Challacombe, Phys. Rev. B **76**, 075112 (2007).
[5] P. M. Celliers, P. Loubeyre, J. H. Eggert, S. Brygoo, R. S. McWilliams, D. G. Hicks, T. R. Boehly, R. Jeanloz, and G. W. Collins, Phys. Rev. Lett. **104**, 184503 (2010).
[6] F. Soubiran, S. Mazevet, C. Winisdoerffer, and G. Chabrier, Phys. Rev. B **86**, 115102 (2012).
[7] F. Soubiran, S. Mazevet, C. Winisdoerffer, and G. Chabrier, Phys. Rev. B **87**, 165114 (2013).
[8] M. A. Morales, J. M. McMahon, C. Pierleoni, and D. M. Ceperley, Phys. Rev. Lett. **110**, 065702 (2013).
[9] G. Huser, N. Ozaki, T. Sano, Y. Sakawa, K. Miyanishi, G. Salin, Y. Asaumi, M. Kita, Y. Kondo, K. Nakatsuka, H. Uranishi, T. Yang, N. Yokoyama, D. Galmiche, and R. Kodama, Phys. Plasmas **20**, 122703 (2013).
[10] D. G. Hicks, P. M. Celliers, G. W. Collins, J. H. Eggert, and S. J. Moon, Phys. Rev. Lett. **91**, 035502 (2003).
[11] P. Drude, Ann. Phys. **306**, 566 (1900).
[12] P. Drude, Ann. Phys. **308**, 369 (1900).
[13] R. Kubo, J. Phys. Soc. Jpn. **12**, 570 (1957).
[14] D. A. Greenwood, Proc. Phys. Soc. **71**, 585 (1958).
[15] D. K. Bradley, J. H. Eggert, D. G. Hicks, P. M. Celliers, S. J. Moon, R. C. Cauble, and G. W. Collins, Phys. Rev. Lett. **93**, 195506 (2004).
[16] P. M. Celliers, G. W. Collins, D. G. Hicks, M. Koenig, E. Henry, A. Benuzzi-Mounaix, D. Batani, D. K. Bradley, L. B. Da Silva, R. J. Wallace, S. J. Moon, J. H. Eggert, K. K. M. Lee, L. R. Benedetti, R. Jeanloz, I. Masclet, N. Dague, B. Marchet, M. Rabec Le Gloahec, C. Reverdin, J. Pasley, O. Willi, D. Neely, and C. Danson, Phys. Plasmas **11**, L41 (2004).
[17] V. B. Mintsev and Y. B. Zaporozhets, Contrib. Plasma Phys. **29**, 493 (1989).
[18] Y. B. Zaporoghets, V. B. Mintsev, V. K. Gryaznov, and V. E. Fortov, in *Physics of Extreme States of Matter*, edited by V. E. Fortov (Inst. Probl. Chem. Phys. RAN, Chernogolovka, 2002), pp. 188–189 [in Russian] .
[19] Y. B. Zaporoghets, V. B. Mintsev, V. K. Gryaznov, V. E. Fortov, H. Reinholz, and G. Röpke, in *Physics of Extreme States of Matter*, edited by V. E. Fortov (Inst. Probl. Chem. Phys. RAN, Chernogolovka, 2004), pp. 140–141 [in Russian] .
[20] Y. Zaporoghets, V. Mintsev, V. Gryaznov, V. Fortov, H. Reinholz, T. Raitza, and G. Röpke, J. Phys. A Math. Gen. **39**, 4329 (2006).
[21] W. Ebeling, Physica **43**, 293 (1969).
[22] H. Reinholz, G. Röpke, A. Wierling, V. Mintsev, and V. Gryaznov, Contrib. Plasma Phys. **43**, 3 (2003).

[23] M. A. Berkovsky, Y. K. Kurilenkov, and H. M. Milchberg, Phys. Fluids B **4**, 2423 (1992).

[24] S. A. Magnitskiy, I. V. Morozov, G. E. Norman, and A. A. Valuev, J. Phys. A: Math. Gen. **36**, 5999 (2003).

[25] H. Reinholz, G. Röpke, I. Morozov, V. Mintsev, Y. Zaparoghets, V. Fortov, and A. Wierling, J. Phys. A Math. Gen. **36**, 5991 (2003).

[26] H. Reinholz, Y. Zaporoghets, V. Mintsev, V. Fortov, I. Morozov, and G. Röpke, Phys. Rev. E **68**, 036403 (2003).

[27] N. A. Medvedev, A. E. Volkov, K. Schwartz, and C. Trautmann, Phys. Rev. B **87**, 104103 (2013).

[28] B. Rethfeld, A. Rämer, N. Brouwer, N. Medvedev, and O. Osmani, Nucl. Instrum. Methods B **327**, 78 (2014).

[29] F. Cheenicode Kabeer, E. S. Zijlstra, and M. E. Garcia, Phys. Rev. B **89**, 100301 (2014).

[30] M. W. C. Dharma-wardana, Phys. Rev. E **86**, 036407 (2012).

[31] W. Kohn and L. J. Sham, Phys. Rev. **140**, A1133 (1965).

[32] Y. Laudernet, J. Clérouin, and S. Mazevet, Phys. Rev. B **70**, 165108 (2004).

[33] J. Clérouin, Y. Laudernet, V. Recoules, and S. Mazevet, Phys. Rev. B **72**, 155122 (2005).

[34] M. P. Desjarlais, Contrib. Plasma Phys. **45**, 300 (2005).

[35] M. Gajdoš, K. Hummer, G. Kresse, J. Furthmüller, and F. Bechstedt, Phys. Rev. B **73**, 045112 (2006).

[36] M. French and R. Redmer, Phys. Plasmas **18**, 043301 (2011).

[37] M. E. Povarnitsyn, D. V. Knyazev, and P. R. Levashov, Contrib. Plasma Phys. **52**, 145 (2012).

[38] Y. Ping, D. Rocca, and G. Galli, Phys. Rev. B **87**, 165203 (2013).

[39] N. D. Mermin, Phys. Rev. **137**, A1441 (1965).

[40] T. R. Mattsson and R. J. Magyar, AIP Conf. Proc. **1195**, 797 (2009).

[41] H. Ehrenreich and M. H. Cohen, Phys. Rev. **115**, 786 (1959).

[42] S. L. Adler, Phys. Rev. **126**, 413 (1962).

[43] N. Wiser, Phys. Rev. **129**, 62 (1963).

[44] A. Starace, Phys. Rev. A **3**, 1242 (1971).

[45] R. Del Sole and R. Girlanda, Phys. Rev. B **48**, 11789 (1993).

[46] V. Recoules, P. Renaudin, J. Clérouin, P. Noiret, and G. Zérah, Phys. Rev. E **66**, 056412 (2002).

[47] D. A. Kirzhnits, Sov. Phys. Uspekhi **19**, 530 (1976).

[48] R. P. Feynman, R. B. Leighton, and M. Sands, *The Feynman Lectures on Physics*, 2nd ed., Vol. 2 (Addison-Wesley Longman, London, 2005), p. 570.

[49] D. V. Sivukhin, *General Physics, Volume 3: Electricity* (Fizmatlit, Moscow, 2004), p. 656 [in Russian].

[50] G. Kresse and J. Hafner, Phys. Rev. B **47**, 558 (1993).

[51] G. Kresse and J. Hafner, Phys. Rev. B **49**, 14251 (1994).

[52] G. Kresse and J. Furthmüller, Phys. Rev. B **54**, 11169 (1996).

[53] G. Kresse and J. Furthmuller, Comput. Mater. Sci. **6**, 15 (1996).

[54] J. P. Perdew, A. Ruzsinszky, G. I. Csonka, O. A. Vydrov, G. E. Scuseria, L. A. Constantin, X. Zhou, and K. Burke, Phys. Rev. Lett. **100**, 136406 (2008).

[55] S. Nosé, J. Chem. Phys. **81**, 511 (1984).

[56] W. G. Hoover, Phys. Rev. A **31**, 1695 (1985).

[57] See Supplemental Material at http://link.aps.org/supplemental/10.1103/PhysRevE.91.023105 for the example of a quantum molecular dynamics trajectory for the xenon plasma DFT model considered.

[58] G. E. Norman and V. V. Stegailov, Math. Models Comput. Simul. **5**, 305 (2013).

[59] M. P. Desjarlais, J. D. Kress, and L. A. Collins, Phys. Rev. E **66**, 025401 (2002).

[60] L. D. Landau and E. M. Lifshitz, in *Electrodynamics of Continuous Media*, edited by E. M. Lifshitz and L. P. Pitaevskii (Pergamon Press, Oxford, 1960), p. 417.

[61] A. Lankin and G. Norman, Contrib. Plasma Phys. **49**, 723 (2009).

[62] A. V. Lankin and G. E. Norman, J. Phys. A Math. Gen. **42**, 214032 (2009).

[63] G. E. Norman, I. M. Saitov, and V. V. Stegailov, Contrib. Plasma Phys. **55**, 215 (2015).

[64] V. Fortov, V. Gryaznov, V. Mintsev, V. Ternovoi, I. Iosilevski, M. Zhernokletov, and M. Mochalov, Contrib. Plasma Phys. **41**, 215 (2001).

[65] E. Bévillon, J. P. Colombier, V. Recoules, and R. Stoian, Phys. Rev. B **89**, 115117 (2014).

[66] V. Stegailov and P. Zhilyaev, Contrib. Plasma Phys. **55**, 164 (2015).

[67] J. P. Perdew, K. Burke, and M. Ernzerhof, Phys. Rev. Lett. **77**, 3865 (1996).

[68] G. Norman, I. Saitov, V. Stegailov, and P. Zhilyaev, Contrib. Plasma Phys. **53**, 300 (2013).

[69] G. Norman, I. Saitov, V. Stegailov, and P. Zhilyaev, Contrib. Plasma Phys. **53**, 503 (2013).